

Robust Metallic Actuators Based on Nanoporous Gold Rapidly Dealloyed from Gold–Nickel Precursors

Chuan Cheng* and Lukas Lühns

Dealloyed nanoporous gold (np-Au) has applications as oxygen reduction catalysis in Li-air batteries and fuel cells, or as actuators to convert electricity into mechanical energy. However, it faces the challenges of coarsening-induced structure instability, mechanical weakness due to low relative densities, and slow dealloying rates. Here, monolithic np-Au is dealloyed from a single-phase $\text{Au}_{25}\text{Ni}_{75}$ solid-solution at a one-order faster dealloying rate, ultra-low residual Ni content, and importantly, one-third more relative density than np-Au dealloyed from conventional $\text{Au}_{25}\text{Ag}_{75}$. The small atomic radius and low dealloying potential of the sacrificing element Ni are intrinsically beneficial to fast produce high relative density np-Au, as predicted by a general model for dealloying of binary alloys and validated by experiments. Stable, durable, and reversible actuation of np-Au takes place under cyclic potential triggering in alkaline and acidic electrolytes with negligible coarsening-induced strain-shift. The thermal and mechanical robustness of bulk np-Au is confirmed by two-order slower ligament coarsening rates during annealing at 300 °C and 45 MPa macroscopic yielding strength distinctive from the typical early onset of plastic yielding. This article opens a rich direction to achieve high relative density np-Au which is essential for porous network connectivity, mechanical strength, and nanostructure robustness for electrochemical functionality.

1. Introduction

Nanoporous metals, which are top-down synthesized by selectively removing of sacrificing elements from alloy precursors via chemical or physical methods, range from lithium to gold, from thin films to bulk samples, and from mono-porous

structures to hierarchical porous structures.^[1] Due to the high specific surface area, nanosized channels, monolithic body versus nanoparticles, excellent electrical conductivity, and mechanical strength versus nanoporous polymers or ceramics, nanoporous metals have wide applications from energy storage/conversion to CO_2 reduction.^[2] Dealloyed nanoporous gold (np-Au), in particular, has been utilized as a model material to study dealloying mechanisms,^[1a,3] nano-mechanics^[4] and electro-chemo-mechanics,^[5] or for applications in electrocatalysis,^[6] supercapacitors,^[7] batteries,^[8] sensors,^[9] and actuators.^[10] These applications rely on the high surface-area-to-volume ratio of np-Au; in other words, a stable nanoporous structure that does not change or decay.

However, structure coarsening of np-Au starts at low temperatures below 100 °C via surface diffusion of Au driven by the high excess surface energy,^[11] as a result, surface area decreases, ligament size increases, and macroscopic volume

shrinks. Coarsening becomes severe during applications, facilitated by electrical, thermal, or chemical triggering.^[12] The structure instability significantly affects the well-functioning, durability, and controllability of np-Au in practice.

Furthermore, due to the low relative density (solid fraction) and poor network connectivity,^[13] np-Au is vulnerable to early onset of plastic yielding, or even continuous plastic deformation upon compressive loading of a few MPa on macroscopic samples,^[14] which can be worse than the predication from Gibson-Ashby's open-foam theory.^[15] This limits applications that require certain structure stiffness to bear and output load such as actuators. Topology simulation and experiments found that it was due to the poor porous network connectivity, in which not all the ligaments or Au atoms had contributed to the structure rigidity, and >30% relative density was necessary for sufficient network connectivity.^[16] However, reported relative densities of np-Au were normally below 30% if the sacrificing elements were sufficiently removed.^[16] The sacrificing elements were normally, chemically more active than the remaining element Au, which would lead to unstable performance or continuous dissolution if not sufficiently removed, such as during electro-chemo-mechanical testing in 1 M HClO_4 electrolyte.^[5] Therefore, it becomes a critical challenge to stabilize the nanostructure against coarsening as well as increasing the mechanical strength, even though a theoretical pathway is implicitly suggested. Moreover, during electrochemical or chemical dealloying for np-Au, less noble

C. Cheng
Energy Innovation Centre
Warwick Manufacturing Group
University of Warwick
Coventry CV4 7AL, UK
E-mail: Chuan.Cheng@warwick.ac.uk

C. Cheng, L. Lühns
Institute of Materials Physics and Technology
Hamburg University of Technology
21073 Hamburg, Germany

 The ORCID identification number(s) for the author(s) of this article can be found under <https://doi.org/10.1002/adfm.202107241>.

© 2021 The Authors. Advanced Functional Materials published by Wiley-VCH GmbH. This is an open access article under the terms of the Creative Commons Attribution-NonCommercial License, which permits use, distribution and reproduction in any medium, provided the original work is properly cited and is not used for commercial purposes.

The copyright line for this article was changed on 17 December 2021 after original online publication.

DOI: 10.1002/adfm.202107241

(sacrificing) elements are selectively etched from the precursor at slow rates of a few nm s^{-1} ,^[17] and therefore, requires one day or more to corrode over an mm thick precursor which restricts scale-up applications.

Np-Au could be dealloyed from different precursors such as Au-Ag,^[3] Au-Pt-Ag,^[12] Au-Cu,^[18] Au-Al,^[19] and Au-Zn.^[20] Au-Ag alloy is most widely used because it forms a solid solution in all compositions, which leads to a homogenous porous structure and crack-free macroscopic samples; while some other precursors may exhibit multi-phases or dendrites which can lead to cracks in dealloyed np-Au, except for few intermetallic compounds.^[21] Thus, competitive precursors besides Au-Ag alloy are rare.

We think suitable np-Au which can face the challenges may be beyond the ones that were dealloyed from conventional precursors. Interestingly, Au-Ni precursors have been overlooked in the field, because only one related article could be possibly found, in which amorphous Au-Ni thin films were first electrodeposited on Si wafers and then electrochemically dealloyed in dilute H_2SO_4 .^[22] The generated np-Au had frequent appearances of cracks.^[22] By all means, it was different from the required precursors that can generate monolithic crack-free np-Au.

Here, by dealloying crystallized Au-Ni solid-solution for the first time, we aim to mitigate three critical challenges of np-Au, which are i) coarsening-induced structure instability, ii) early onset of plastic yielding, and iii) slow dealloying rate.

Benefiting from the smaller atomic radius of Ni than the conventionally used Ag as the sacrificing element, the relative density of np-Au dealloyed from $\text{Au}_x\text{Ni}_{(1-x)}$ is one-third larger than that dealloyed from $\text{Au}_x\text{Ag}_{(1-x)}$, where $0.2 \leq x \leq 0.35$, located in the region of practical interests to achieve monolithic crack-free np-Au. For example, the relative density of np-Au increases from 25–28% to 35–36% when the precursor is changed from $\text{Au}_{25}\text{Ag}_{75}$ to $\text{Au}_{25}\text{Ni}_{75}$. This advantage is striking because it significantly increases the network connectivity and structure robustness against thermal coarsening and mechanical stresses, as confirmed by our experiments. This new type of np-Au is utilized as an electrochemical actuator to demonstrate the long-term stable, durable, and reversible actuation functionality.

Furthermore, benefiting from the lower critical dealloying potential of Au-Ni (≈ 0.6 V vs SHE) than Au-Ag (≈ 1.2 V vs SHE), dealloying is conducted below potentials for anodic oxidation of Au and oxygen bubbling, both of which could slow down the dealloying rate; as a result, the dealloying rate is significantly elevated ≈ 10 times, from the previous few nm s^{-1} to 98 nm s^{-1} . In other words, it reduces the synthesis time from a commonly used 1 day to 1 h for 3D mm-sized np-Au, plus no time-consuming, post-dealloying is required to further reduce the residual sacrificing element content, because it is already below 1 at%.

These features indicate a new type of np-Au generated from a new precursor unexploited before, that leads to distinguishable mechanical and electrochemical properties due to the high relative density and network connectivity in np-Au, and that can be much faster dealloyed and possibly extends the present bulk size from mm^3 to cm^3 . Bear in mind that Au-Ni solid-solution can be obtained at all possible composition ratios via heat-treatment according to the phase diagram, which indicates vast opportunities for further exploration.

Fabrication methods and predication equations presented in this article could become a general strategy to increase relative

densities in other dealloyed nanoporous metals, especially for those which cannot rely on increasing noble (remaining) metal content in precursors to increase relative density, either because of the dealloying parting limit (e.g., ≈ 45 at% Au for Au-Ag alloy)^[17b] or because crack-free monolithic nanoporous metals could not be obtained at high noble metal contents (e.g., > 35 at% Au for Au-Ag alloy).^[13] With the increase of at% Au in the precursor, it becomes more difficult to obtain fully dealloyed and crack-free bulk np-Au. It is because when Ag atoms are dissolved and leave terrace vacancies, Au atoms will diffuse to the vacancies and prevent further dissolution. With more Au content, it becomes harder for the Ag dissolution rate to surpass the Au diffusion rate and move the dealloying front forward; as a consequence, it will require increased dealloying potentials,^[3] higher dealloying temperatures, or prolonged dealloying time (e.g., 25 days chemical dealloying for $\text{Au}_{35}\text{Ag}_{65}$).^[13] Even though, it was reported that crack-free bulk np-Au could not be electrochemically dealloyed from $\text{Au}_{35}\text{Ag}_{65}$ while only $\text{Au}_{30}\text{Ag}_{70}$ was possible.^[13] Therefore, alternative solutions which can lead to a high relative density in np-Au based on a relatively low Au content in the precursor become important, such as this article presented.

2. Results and Discussion

2.1. Fast Dealloying of Monolithic Bulk Nanoporous Gold from $\text{Au}_{25}\text{Ni}_{75}$ Solid-Solution

$\text{Au}_{25}\text{Ni}_{75}$ ingot was cast by arch-melting in Ar from pure Au and Ni metals. According to the phase diagram of Au-Ni alloy,^[23] a broad region of single-phase solid-solution exists above the miscibility gap and below about 950°C at all compositions, as marked by (Au, Ni) in **Figure 1a**. A single-phase precursor is necessary to obtain narrowly distributed pore/ligament sizes, rather than multi alloy phases that could lead to cracks in dealloyed np-Au. To realize this, the as-cast $\text{Au}_{25}\text{Ni}_{75}$ was heat-treated within the solid-solution region at 900°C for 24 h and then quenched in water. The X-ray diffraction (XRD) pattern of $\text{Au}_{25}\text{Ni}_{75}$ confirms a single-phase fcc crystal structure with a lattice constant of 3.701\AA (**Figure 1b**), which is between the lattice constants of Ni 3.517\AA and Au 4.070\AA .^[24] Noting that, without the heat treatment, $\text{Au}_{25}\text{Ni}_{75}$ alloy with Au-rich and Ni-rich phases would be obtained.^[25]

3D mm-sized $\text{Au}_{25}\text{Ni}_{75}$ precursors were dealloyed in an electrochemical cell (**Figure 1d**). See Experimental Section for setup. Because Au-Ni solid-solution has not been dealloyed before, dealloying conditions are determined here. Conventional Au alloy precursors such as Au-Ag, Au-Cu, and Au-Pt-Ag were dealloyed by strong oxidizing acids of HClO_4 and HNO_3 ,^[17a,18] however, we found that HClO_4 was impossible to leach out Ni from $\text{Au}_{25}\text{Ni}_{75}$ due to the strong passivation from 0.63 to 1.80 V versus SHE, even beyond the O_2 evolution limit (1.23 V vs SHE), as shown in **Figure 1e** (black). Instead, we found that the strong but non-oxidizing acid of HCl can effectively dealloy $\text{Au}_{25}\text{Ni}_{75}$ above a critical potential of 0.60 V vs SHE (**Figure 1e**, red). The critical potential defines the onset of dealloying where the current quickly rises and the surface of the precursor transforms from smooth to porous.^[26] This critical dealloying potential

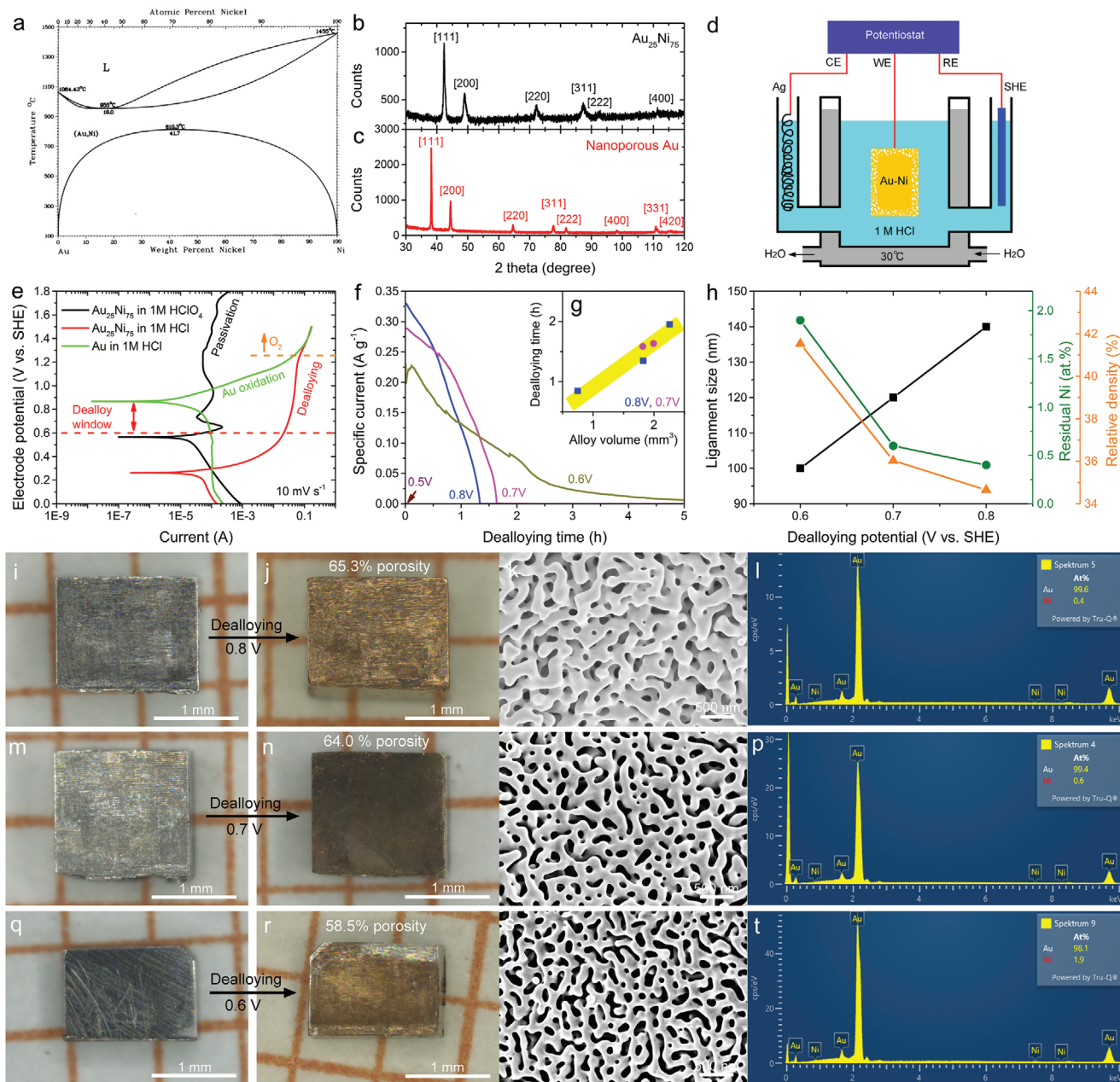


Figure 1. Bulk nanoporous gold (np-Au) fast dealloyed from $\text{Au}_{25}\text{Ni}_{75}$ solid-solution. a) Phase diagram of Au-Ni alloy. Reproduced with permission,^[23] copyright 2016, ASM International. b, c) XRD of $\text{Au}_{25}\text{Ni}_{75}$ (black) and np-Au (red). d) Illustration of an electrochemical dealloying setup. e) Potentiodynamic behavior of $\text{Au}_{25}\text{Ni}_{75}$ (surface area $\approx 0.61 \text{ cm}^2$) in 1 M HCl and 1 M HClO_4 at 10 mV s^{-1} , and pure Au in 1 M HCl. f) Specific current versus dealloying time at 0.5, 0.6, 0.7, and 0.8 V versus SHE, respectively, in 1 M HCl at 30°C . g) Total dealloying time versus precursor volume at 0.7 and 0.8 V. h) Ligament size (black), residual Ni at% (green), and relative density of np-Au versus dealloying potential. i, m, q) Photos of bulk $\text{Au}_{25}\text{Ni}_{75}$ precursors; j, n, r) the corresponding np-Au dealloyed at 0.8, 0.7, and 0.6 V; k, o, s) the corresponding SEM images and l, p, t) EDX element analysis of as-dealloyed np-Au.

is much lower than that for $\text{Au}_{25}\text{Ag}_{75}$ ($\approx 1.2 \text{ V vs SHE}$)^[3] and $\text{Au}_{25}\text{Cu}_{75}$ ($\approx 1.2 \text{ V vs SHE}$).^[18] The low critical dealloying potential enables the $\text{Au}_{25}\text{Ni}_{75}$ to evade the anodic oxidation of Au ($>0.87 \text{ V vs SHE}$, Figure 1e, green). Au oxidation may either hinder the surface diffusion and slow down the dealloying rate, or lead to Au dissolution in HCl^[27] and weaken the mechanical strength of np-Au. As such, a proper dealloying window should be between 0.60 and 0.87 V versus SHE in 1 M HCl, as noticed by red arrows in Figure 1e.

Next, a series of potentiostatic dealloying were conducted around the dealloying window, at 0.5, 0.6, 0.7, and 0.8 V versus SHE in 1 M HCl at 30°C . Except for 0.5 V, at which no dealloying current could be observed, the specific current decreases monotonically towards zero with time (Figure 1f). Especially for 0.7 and 0.8 V, at which the current steeply reduces to zero after only 1.6 and 1.3 h for bulk precursors of $\approx 1.5 \times 1.4 \times 0.9 \text{ mm}^3$, and correspond to dealloying rates of 78 nm s^{-1} ($= 0.45 \text{ mm} / 1.6 \text{ h}$) and 96 nm s^{-1} ($= 0.45 \text{ mm} / 1.3 \text{ h}$), respectively. At 0.6 V,

although the precursor is smaller ($\approx 1.5 \times 1.0 \times 0.5 \text{ mm}^3$), the dealloying time is still $\approx 5 \text{ h}$. Therefore, 0.7 and 0.8 V are preferred for fast dealloying. Quantitatively, from the yellow region of Figure 1g, there is an approximately linear relationship between total dealloying time and volume of the bulk precursor, from which the dealloying time is $\approx 0.8 \text{ h per mm}^3$ precursor.

The dealloying time is extremely shorter than dealloying similar-sized Au-Ag precursors, such as 20 h at 1.28 V versus SHE in 1 M HClO₄ for Au_pAg_{100-p} ($p = 23, 25, 27, 35$; $\approx 1.0 \times 1.0 \times 1.8 \text{ mm}^3$);^[17a] 24 h at 1.29 V versus SHE in 1 M HClO₄ for Au₂₈Ag₇₂ ($\approx 2 \text{ mm} \times 1 \text{ mm}$ diameter).^[28] The estimated dealloying rate for Au-Ag is $\approx 7 \text{ nm s}^{-1}$ ($0.5 \text{ mm} / 20 \text{ h}$), which is 10 times slower than our Au-Ni dealloyed at 0.7 and 0.8 V. Also, a typical dealloying rate for Au-Ag in concentrated HNO₃ was only 1 nm s^{-1} ,^[29] and 10 days dealloying was required.^[17a] For more active metals, such as nanoporous Ni dealloyed from Ni-Mn alloy, a dealloying rate was also a few nm s^{-1} , e.g., 20–30 h for similar-sized bulk samples.^[30] Therefore, the ultra-fast dealloying rate presented here is remarkable among electrochemical and chemical dealloying of metals.

After dealloying, the white metal Au₂₅Ni₇₅ (Figure 1i,m,q) changed to golden-colored np-Au (Figure 1j,n,r). XRD of np-Au dealloyed at 0.8 V is shown in Figure 1c, which exhibits a simple peak shift compared with the precursor (Figure 1b) and indicates the same fcc crystal structure. The lattice constant of np-Au is 4.077 \AA corresponding to pure Au.^[24] The as-dealloyed np-Au was cut by a knife to view the cross-section in a scanning electron microscope (SEM). No un-dealloyed solid core can be found in the sample (Figure S1, Supporting Information).

SEM images show bi-continuous nanoporous structures in np-Au (Figure 1k,o,s). The ligament and pore sizes are measured from SEM images by ImageJ^[31] and statistically evaluated (Figure S2, Supporting Information). At each dealloying condition, both ligament and pore sizes have narrow distributions with $\approx 20\%$ deviation around the average. The ligament size increases linearly with dealloying potential from $100 \pm 21 \text{ nm}$ to $140 \pm 31 \text{ nm}$ (Figure 1h, black).

Energy-dispersive X-ray spectroscopy (EDX) was commonly used to determine residual element content in np-Au because the information depth of EDX ($\approx 1 \mu\text{m}$) was much larger than the ligament size.^[28] Remarkably, at such a fast dealloying rate, the residual Ni is negligibly small, i.e., $<1 \text{ at\%}$ for 0.7 and 0.8 V, and $<2 \text{ at\%}$ for 0.6 V (Figure 1i,p,t). Nevertheless, it is consistent with XRD of np-Au which corresponds to pure Au (Figure 1c), and also consistent with EDX of the annealed np-Au (Figure S3, Supporting Information).

Differently, to reach a low residual Ag content $\leq 1 \text{ at\%}$ with similar-sized Au₂₅Ag₇₅ precursors, post-dealloying at higher anodic potentials were required, such as 1.53 V versus SHE for 2 h after dealloying at 1.23 V versus SHE for 20 h;^[17a] three post-dealloying steps with $>8 \text{ h}$ in each step after dealloying at 1.29 V versus SHE for 24 h.^[28] The post-dealloying not only consumes more time but also further reduces the relative density of np-Au, normally below 30%.^[16–17] The relative density equals np-Au density divided by solid Au density. In contrast, with a one-step fast dealloying, the relative densities are all above 34% (Figure 1h, orange).

The fast dealloying rate could originate from three aspects. First, dealloying is a kinetic competition between surface

diffusion of more noble elements and dissolution of less noble elements at the dealloying front,^[17b] while chloride-containing electrolyte can facilitate both surface diffusion of Au^[17b,32] and dissolution of Ni.^[33] The strong non-oxidation HCl acid prevents surface passivation. Second, the standard electrode potential of Ni²⁺/Ni (-0.257 V vs SHE) is much smaller than Ag⁺/Ag (0.799 V vs SHE), which leads to a low critical dealloying potential for Au₂₅Ni₇₅ ($\approx 0.6 \text{ V vs SHE}$), only 50% for Au₂₅Ag₇₅ ($\approx 1.2 \text{ V vs SHE}$).^[3] As a result, dealloying was conducted below potentials of Au oxidation and oxygen evolution, while these processes may hinder surface diffusion and mass transport at the dealloying front. Indeed, the as-dealloyed np-Au from Au₂₅Ag₇₅ at 1.3 V versus SHE in 1 M HClO₄ was covered with surface oxides, which can be removed by reduction at lower potentials (e.g., Figure 3a in ref. [34]).

2.2. Stable, Durable, and Reversible Electrochemical Actuation of Bulk Nanoporous Gold

In Figure 2, bulk np-Au dealloyed from Au₂₅Ni₇₅ are utilized as electrochemical actuators. Charge-induced reversible volume change takes place during charging-discharging of the np-Au electrode. The uniaxial actuation strain ($\Delta L/L_0$) was measured in situ by a dilatometer (Figure 2c), where L_0 is the initial sample length and ΔL is length change. See Experimental Section for setup. Two np-Au dealloyed at the same condition (0.7 V, 30 °C) and with the ligament size of $\approx 120 \text{ nm}$ were actuated in 1 M H₂SO₄ and 1 M NaOH, respectively. Figure 2a shows that their cyclic voltammetry (CV) behave differently because the onset of Au oxidation shifts with the pH of the electrolytes.^[35] Both CVs can be separated into two regions, i.e., a double-layer region with capacitive charge accumulated at the surface, and a pseudo-capacitive region with ion adsorption and Au oxidation at the surface.^[36]

Before charging, the interatomic distance among surface atoms is shorter than that in the substrate due to the redistribution of surface electrons towards the inner bonds.^[37] Upon capacitive double-layer charging, the excess positive charge reduces surface electron density and relaxes interatomic distances, which leads to localized surface expansion.^[37] Upon pseudo-capacitive charging, the newly formed oxides further expand the surface in comparison to the substrate. These processes are reversible during discharging. The nanoporous structure converts localized interatomic change into macroscopic dimension change of bulk np-Au, as a result, np-Au expands during positive potential scanning and reversibly shrinks during negative scanning (Figure 2d).

Strain hysteresis mainly takes place in pseudo-capacitive charging which is rate-limited by ion diffusion.^[38] As such, the induced strain tends to decrease with scan rate from 1 to 25 mV s^{-1} (Figure 2b,d). Further, the strain decreases faster in 1 M NaOH than in 1 M H₂SO₄, because the diffusion coefficient of OH⁻ is smaller than H⁺ in aqueous electrolytes.^[39] Accordingly, the pseudo-capacitive charge integrated from CV also decreases more quickly with scan rate in 1 M NaOH than in 1 M H₂SO₄ (x -axis of Figure 2e,f), which corresponds to a faster strain reduction.

Actuation stability of np-Au is reflected by a long-term continuous actuation in 1 M H₂SO₄ at scan rates from 2000 to 1 mV s^{-1}

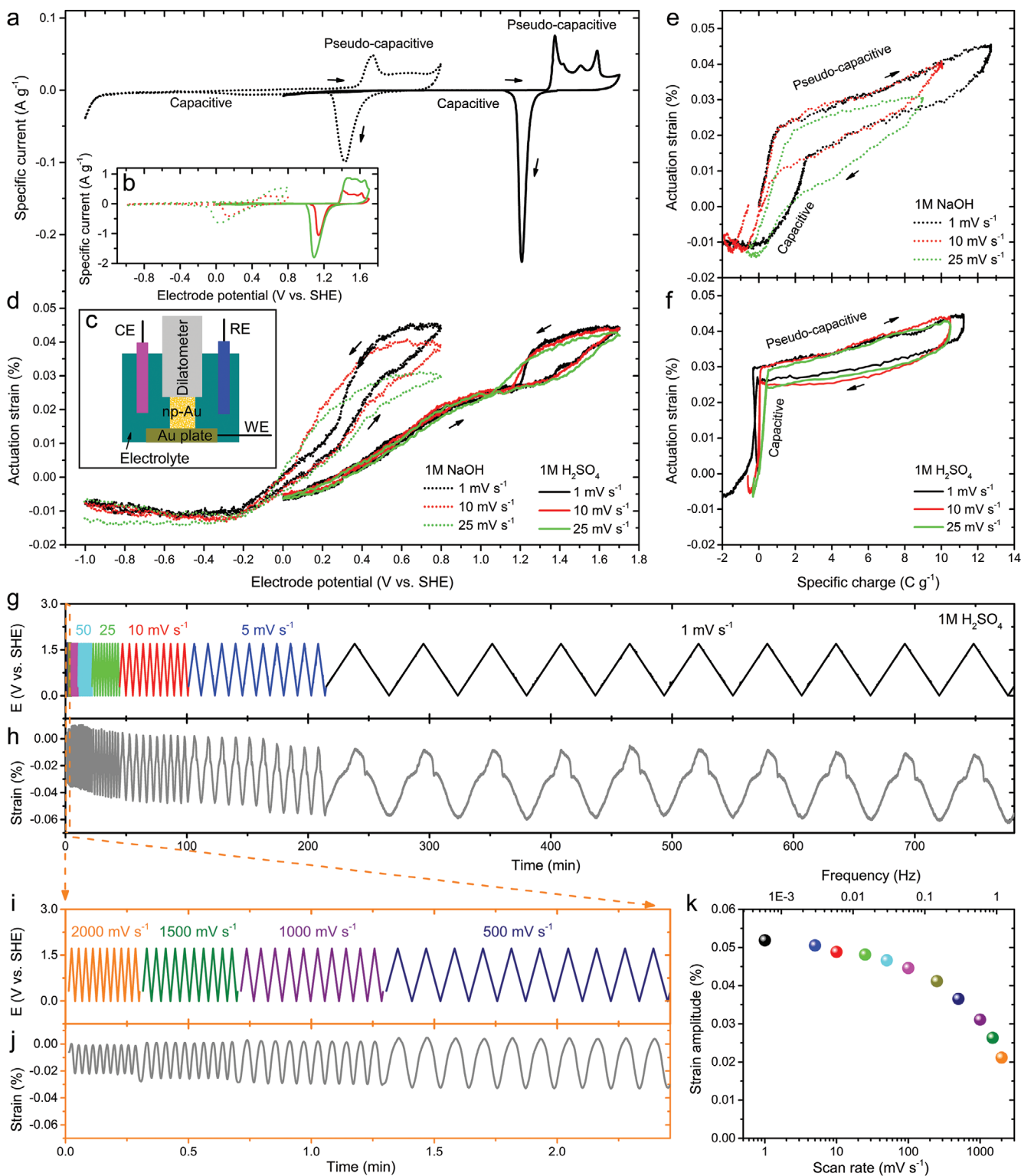


Figure 2. In situ electrochemical actuation of np-Au with ligament size of 120 nm. a,b) Cyclic voltammetry of np-Au in 1 M NaOH and 1 M H_2SO_4 , respectively, at 1 $mV\ s^{-1}$ (black), 10 $mV\ s^{-1}$ (red), and 25 $mV\ s^{-1}$ (green). c) Illustration of a setup for in situ actuation measurement. d) Actuation strain of np-Au versus electrode potential corresponding to (a,b). e,f) Actuation strain versus specific charge measured in 1 M NaOH and 1 M H_2SO_4 , respectively. g,h) 13 h successive actuation of np-Au in 1 M H_2SO_4 , scanned within [0, 1.7] V versus SHE at rates from 2000 to 1 $mV\ s^{-1}$, and conducted 10 cycles at each rate. i,j) An enlarged time region to see details at fast scan rates $\geq 500\ mV\ s^{-1}$. k) Actuation strain amplitude as a function of scan rate and frequency.

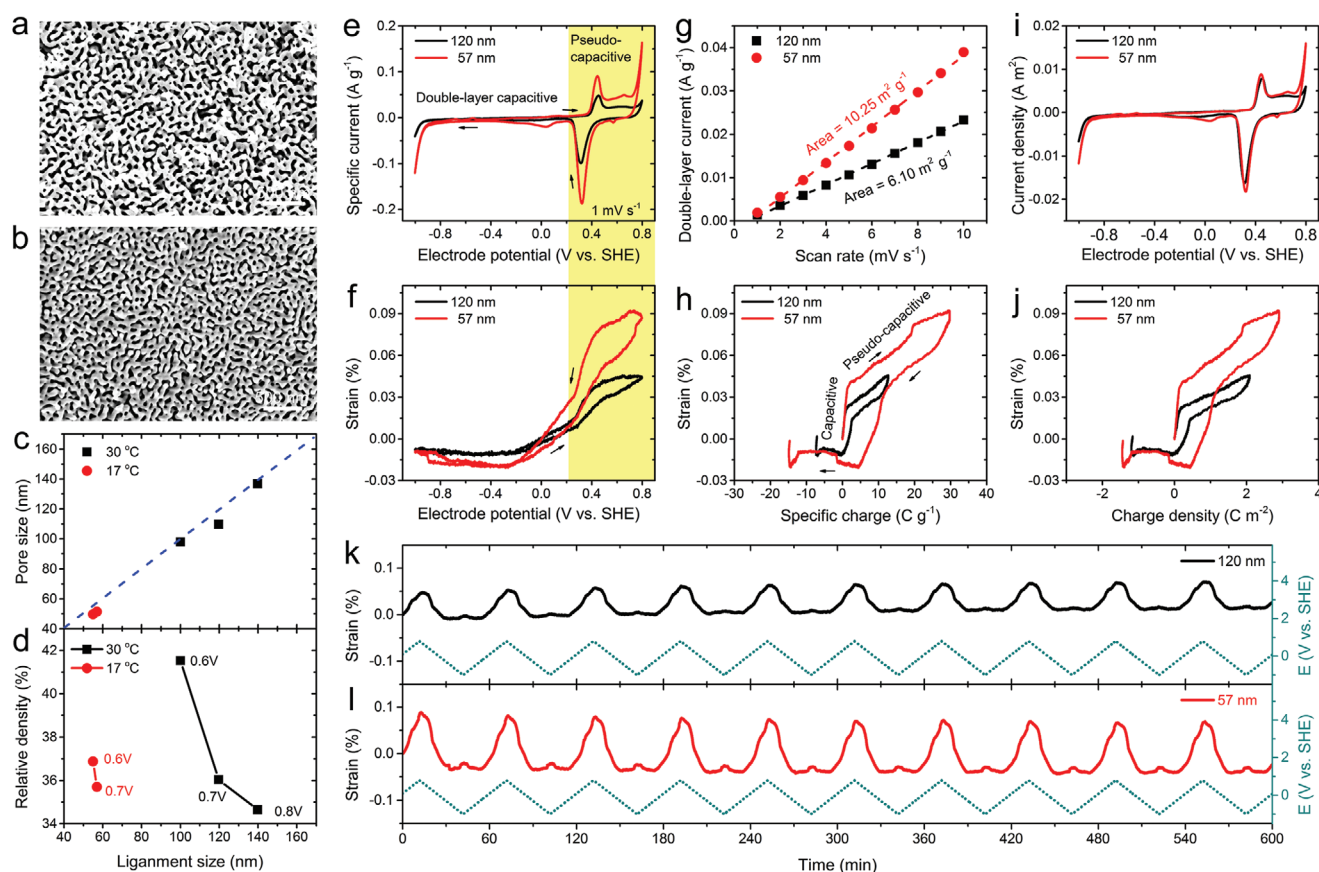


Figure 3. Ligament size-dependent electrochemical actuation of np-Au. a, b) SEM of np-Au dealloyed at 0.6 and 0.7 V versus SHE, respectively, in 1 M HCl at 17 °C. c) Ligament size versus pore size in as-dealloyed np-Au. d) Relative density versus ligament size. e) Cyclic voltammetry of np-Au with ligament sizes of 120 and 57 nm in 1 M NaOH at 1 mV s⁻¹, and f) the corresponding actuation strain versus electrode potential. g) Current intensity at the double-layer versus scan rate for surface area measurement. h) Actuation strain as a function of the specific charge. i, j) correspond to (e, h) after normalizing current and charge with the surface area of np-Au. k, l) Reversible and stable actuation of np-Au during cyclic potential scanning at 1 mV s⁻¹ for 10 h.

with 10 cycles at each rate (Figure 2g–j). During 13 h actuation, a strain-shift of 1.46×10^{-4} is detected, which is less than the minimum reversible strain at 2000 mV s⁻¹ (2.10×10^{-4}). This actuation stability is remarkable because strain-shift was a typical issue for previous np-Au actuators; and even with the help of Pt additive that had a slower diffusion rate than Au, the strain-shift was over 10 times larger than the reversible strain itself within 6 h actuation (Figure 1 in ref. [12]). Accompanied with strain-shift is irreversible volume shrinkage and surface area reduction, which are detrimental to the stable performance and controllability of actuators.

Similar to other electrochemical actuators, sluggish ion diffusion restricts the pseudo-capacitive charging, which leads to the reduction of strain amplitude towards the double-layer-charge induced strain.^[40] From 0.001 to 1 Hz, the strain amplitude reduces $\approx 50\%$ from 5.19×10^{-4} to 2.43×10^{-4} (Figure 2k). At a certain frequency (or scan rate), the strain amplitude is stable and reversible during repeated cycles (Figure 2j).

For comparison of actuation amplitudes, a np-Au dealloyed from Au₂₅Ag₇₅ had a ligament size of 55 nm and exhibited a strain of $\approx 2.0 \times 10^{-4}$ at 10 mV s⁻¹ scan rate in 1 M HClO₄.^[5a] Although our ligament size is much larger (120 nm, Figure 2), the strain amplitudes at the same scan rate are two times more,

i.e., 5.0×10^{-4} (in 1 M H₂SO₄) and 5.2×10^{-4} (in 1 M NaOH). For a np-Au dealloyed from Au₂₅Ag₇₅ and annealed to the same ligament size of 120 nm, the strain amplitude was 4.7×10^{-5} at 10 mV s⁻¹,^[41] i.e., only one-tenth of our samples. The large strain amplitude here should be attributed to the high relative density (36%, Figure 2) than previously reported np-Au (25% in ref. [5a] and 27% in ref. [41]), which leads to good network connectivity so that more effective ligaments contribute to the macroscopic volume change, rather than dangling ligaments^[42] that have free-ends and do not carry loads or contribute to the structure stiffness (see later for details).

Ligament sizes of np-Au dealloyed from Au₂₅Ni₇₅ can be significantly reduced by decreasing dealloying temperature. The ligament size decreases $\approx 50\%$ with temperature decreased from 30 to 17 °C, i.e., from 100 ± 21 nm (Figure 1s) to 55 ± 11 nm at 0.6 V (Figure 3a), and from 120 ± 29 nm (Figure 1o) to 57 ± 12 nm at 0.7 V (Figure 3b). Following this trend, even smaller ligament sizes could be obtained. At 17 °C and 0.7 V, the dealloying rate is 64 nm s⁻¹, i.e., 1.3 h dealloying time for $\approx 1.3 \times 0.9 \times 0.6$ mm³ sized precursor, which is still 9 times the rate for Au₂₅Ag₇₅ precursors (≈ 7 nm s⁻¹).^[17a] Also, no time-consuming, post-dealloying process is required to reduce residual Ni, as it is already down to 1 at% (Figure S3d, Supporting

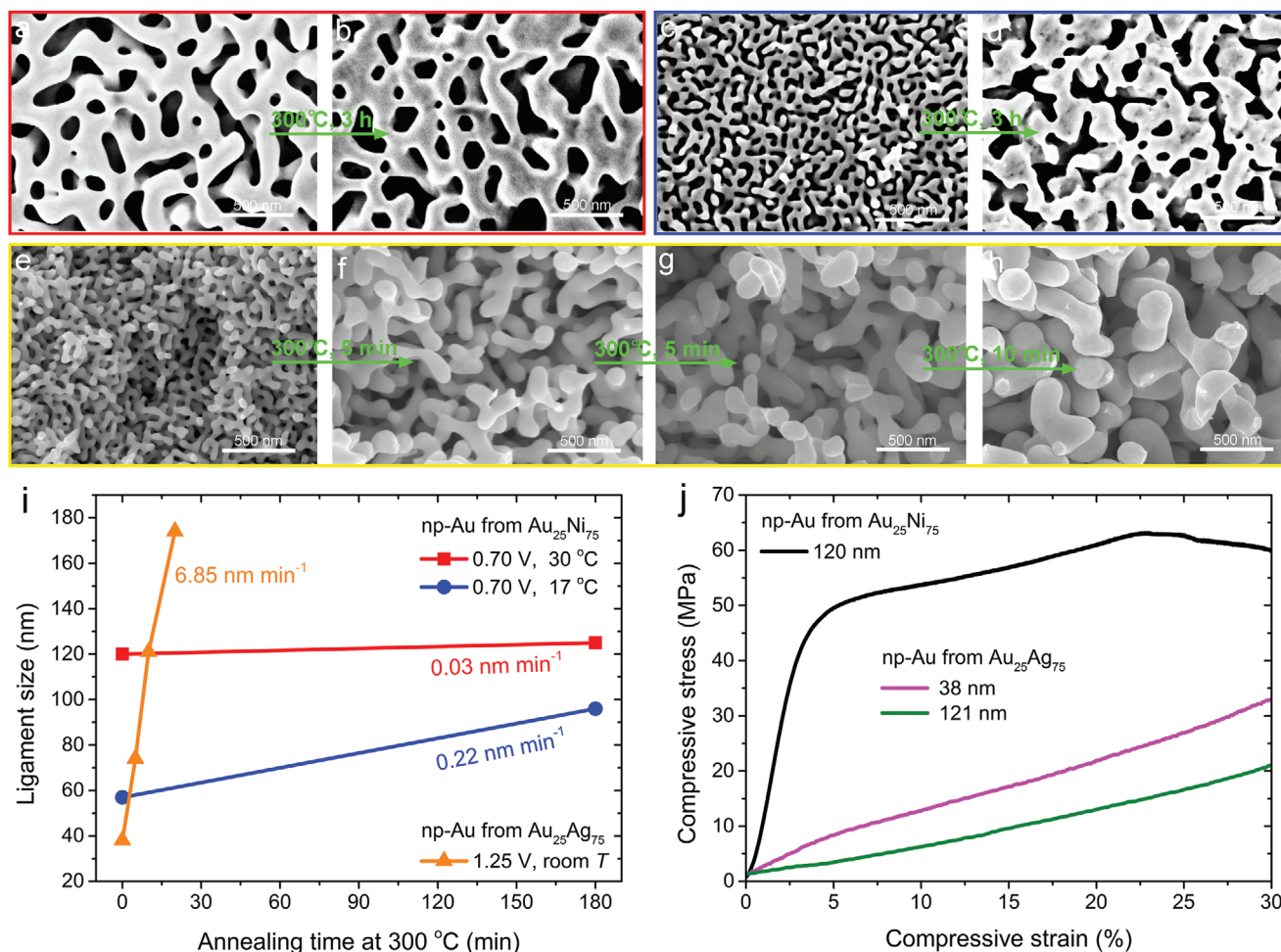


Figure 4. Thermally and mechanically robust bulk np-Au dealloyed from Au₂₅Ni₇₅ in comparison with bulk np-Au dealloyed from Au₂₅Ag₇₅. a) As-dealloyed np-Au from Au₂₅Ni₇₅ at 0.7 V versus SHE in 1 M HCl at 30 °C, and b) after annealing at 300 °C for 3 h. c) As-dealloyed np-Au from Au₂₅Ni₇₅ at 0.7 V versus SHE in 1 M HCl at 17 °C, and d) after annealing at 300 °C for 3 h. e) As-dealloyed np-Au from Au₂₅Ag₇₅ at 1.25 V versus SHE in 1 M HClO₄ at room temperature, and f–h) after annealing at 300 °C for 5, 10, and 20 min (e), respectively. The differences in annealing time between two neighboring figures are noticed. All SEM images have the same amplification. i) Ligament size of np-Au versus annealing time at 300 °C. j) Compressive stress-strain curves of bulk np-Au measured by uniaxial compression tests at 10⁻⁴ s⁻¹ strain rate. The black curve corresponds to (a). The pink and green curves correspond to (e,g), respectively.

Information). The pore size (diameter) of as-dealloyed np-Au is slightly smaller than the ligament size (Figure 3c). The relative densities of np-Au obtained at 17 °C are above 35% (Figure 3d).

Ligament size affects the specific surface area and the actuation performance of np-Au. Two np-Au with 57 and 120 nm ligament sizes are investigated. They have similar relative densities of ≈36% (Figure 3d, 0.7 V). Reversible actuation is detected in both samples during CV at 1 mV s⁻¹ in 1 M NaOH (Figure 3e,f). The strain amplitude increases from 0.05 to 0.10% with ligament size decreasing from 120 to 57 nm.

Charge integrated from the CV is not conservative between positive and negative potential scanning (Figure S4, Supporting Information), due to the charge loss at the potential ends that attribute to H₂ evolution (<-0.826 V vs SHE) and O₂ evolution (>0.404 V vs SHE) according to the Pourbaix diagram at pH = 14.^[35] Because of this, not all the consumed charges contribute to the actuation. But we can still use the specific charge

versus strain plot (Figure 3h) to distinguish strain that is induced by capacitive double-layer charge and pseudo-capacitive charge.

The surface area of np-Au is electrochemically determined,^[34] where the area equals double-layer capacity divided by the double-layer capacitance. The double-layer capacity equals the current intensity at the double-layer (Figure S5, Supporting Information) divided by scan rate, i.e., the line slope in Figure 3g. The double-layer capacitance of Au (≈40 μF cm⁻²) refers to Figure 3a in ref. [43]. As a result, the specific surface areas are 6.10 and 10.25 m² g⁻¹ for the np-Au with a ligament size of 120 and 57 nm, respectively.

As expected, a smaller ligament size leads to a larger specific surface area, which results in a higher specific current (Figure 3e) and a higher specific charge (Figure 3h, x-axis). As such, when the surface area is normalized, the current densities of the two samples approximately overlap with each other (Figure 3i); however, the two strain curves do not overlap (Figure 3j), even though the charge densities are close

(Figure 3j, x-axis). In other words, the np-Au with a smaller ligament size (57 nm) is more effective to utilize the same amount of charge to generate a larger actuation strain. This is the strain amplification effect of a more curved (or rough) electrode surface that restricts in-plane relaxation of surface stresses compared with a smoother surface, as we reported before elsewhere.^[44]

During long-term actuation for 10 h, reversible and stable actuation takes place for both np-Au samples (Figure 3k,l), in which negligible strain-shift can be observed, although the 57 nm ligament would be more likely to coarsen than the 120 nm ligament, it did not. The stable actuation of our np-Au is mainly attributed to the high relative density $\approx 36\%$ (Figure 3d), which guarantees network connectivity and structure robustness against coarsening, as investigated in the following sections.

2.3. Proof of Thermal and Mechanical Robustness of Bulk Nanoporous Gold

To compare the structure robustness against thermal coarsening and compressive stresses, np-Au dealloyed from both Au₂₅Ni₇₅ and Au₂₅Ag₇₅ were tested. For a np-Au dealloyed from Au₂₅Ni₇₅ (Figure 4a), after annealing at 300 °C for 3 h, the ligament size only increases 4% from 120 ± 29 nm to 125 ± 33 nm (Figure 4b), which corresponds to a ligament growth rate of 0.03 nm min⁻¹. For a np-Au with a smaller ligament size of 57 ± 12 nm (Figure 4c), after the same annealing, the ligament size increases 68% to 96 ± 25 nm (Figure 4d) and corresponds to a growth rate of 0.22 nm min⁻¹ (Figure 4i, blue).

In contrast, for a np-Au dealloyed from Au₂₅Ag₇₅, the ligament size increases from 38 ± 9 nm (Figure 4e) to 74 ± 18 nm (Figure 4f), to 121 ± 31 nm (Figure 4g), and to 174 ± 40 nm (Figure 4h) after annealing at 300 °C for 5, 10, and 20 min, respectively. From Figure 4e–h, the ligament size increases 358% in only 20 min, and corresponds to a growth rate of 6.85 nm min⁻¹ (Figure 4i, orange), which is ≈ 30 and ≈ 340 times faster than np-Au dealloyed from Au₂₅Ni₇₅ in Figure 4i (blue) and Figure 4i (red), respectively. Starting from the same ligament size of ≈ 120 nm in Figure 4a,g, the former ligament growth rate is 175 times slower than the latter during annealing at 300 °C. According to literature,^[45] ligament size increases with coarsening time and the coarsening rate exhibits an Arrhenius-type temperature dependence

$$d^n - d_0^n = tC \exp\left(-\frac{E_a}{RT}\right) \quad (1)$$

where d is the annealed ligament size, d_0 is the initial ligament size, n is an exponent varying the range of 3 to 4,^[45] t is coarsening time, C is a constant, E_a is the activation energy for coarsening, R is gas constant, and T is coarsening temperature. According to Herring's scaling law,^[46] $n = 4$ represents a self-similar coarsening controlled by surface diffusion, while $n = 3$ represents a volume diffusion controlled process.

The anti-coarsening robustness is attributed to the high relative density of np-Au dealloyed from Au₂₅Ni₇₅ ($\approx 36\%$ in Figure 4a,c), which is much larger than that dealloyed from Au₂₅Ag₇₅ (25% in Figure 4e). Higher relative density promotes

better porous network connectivity, in which fewer dangling (free-end) ligaments exist.^[16–17] For example, by comparing Figure 4a,g, although they have a similar ligament size of ≈ 120 nm, Figure 4g shows more dangling ligaments. It is because when the relative density is below a threshold of 30%,^[16–17] network connectivity will become worse through ligament pitch-off,^[47] in which a ligament breaks at the middle and creates two dangling ligaments. Even for np-Au dealloyed from Au-Ni, such as Au₁₀Ni₉₀ in Figure S6 in the Supporting Information, dangling ligaments also frequently appear due to the low relative density of 22%, which is detrimental to the network connectivity. In addition, the residual Ni, although has a low content (<1 at%), may also contribute to slow down the thermal coarsening rate of np-Au controlled by surface diffusion. The activation energy for surface diffusion of Ni was ≈ 90 kJ mol⁻¹,^[48] which was larger than that for Au (e.g., 62 ± 8 kJ mol⁻¹ for Au)^[49] and Ag (e.g., ≈ 78 kJ mol⁻¹).^[45c] Therefore, Ni is harder to be activated than both Au and Ag during coarsening.

The anti-coarsening robustness goes hand-in-hand with the mechanical strength of np-Au, which is also critical for actuators that require certain strength to bear and output load. For a np-Au dealloyed at the same condition as Figure 4a, elastic to plastic deformation happened at 4% compressive strain with a yielding strength of 45 MPa (Figure 4j, black, 120 nm). Differently, for a np-Au having a similar ligament size, but dealloyed from Au₂₅Ag₇₅, no obvious yielding point could be found even when the strain increases beyond 30% (Figure 4j, green, 121 nm); instead, it shows a continuous plastic deformation once upon compressive stresses. Even considering the smaller ligament size the stronger effect,^[50] for a np-Au dealloyed from Au₂₅Ag₇₅ with a ligament size of 38 nm (Figure 4j, pink),^[51] the yielding point appears roughly at 4% compressive strain with a yielding strength of ≈ 9 MPa, i.e., only one-fifth of that dealloyed from Au₂₅Ni₇₅.

During similar compressive tests, bulk np-Au dealloyed from Au-Ag precursors experienced early onset of plastic yielding,^[14a] yielding started at low stresses below a few MPa (e.g., Figure 2b in ref. [14a]), or immediate plastic yielding happened even at the lowest strain with no distinguishable yield point (e.g., Figure 2a in ref. [14b], Figure 4 in ref. [52]). These features are consistent with the comparison samples in Figure 4j (pink, green), but obviously different from the robust behavior shown in Figure 4j (black).

The distinguishable high yielding strength of np-Au dealloyed from Au₂₅Ni₇₅ is also attributed to the high relative density, i.e., 36% in Figure 4j (black) versus 25% in Figure 4j (pink) and 28% in Figure 4j (green). According to Gibson-Ashby's open-foam theory,^[15] the macroscopy yielding strength (σ_y) links to the relative density of np-Au (ϕ) by, $\sigma_y = C_1 \sigma_0 \phi^{3/2}$, where $C_1 = 0.3$ for np-Au,^[13] and σ_0 is the yield strength of solid Au. The small relative density below a threshold of 30% further reduces network connectivity of np-Au,^[16–17] as a result, the mechanical strength became even less than the prediction from Gibson-Ashby's theory (e.g., Figures 2e and 3b in ref. [14a]).

The network connectivity can be quantitatively characterized by genus, i.e., the maximum number of cuts that can be made through a network structure before it splits into two parts.^[47] Genus can be measured through the 3D topology of np-Au,^[53] which is out of the scope of this article. However, according to

publications, the genus of np-Au first exponentially increased with relative density; and above 30% relative density, the genus approached steady-state values indicating sufficient network connectivity (e.g. Figure 6 in ref. [16]); while, Young's modulus (Y) of np-Au was proportional to both genus (g) and relative density (φ), by, $Y = C_2 g^{4/3} \varphi^2 Y^0$, where C_2 is a constant and Y^0 is Young's modulus of solid Au.^[17a] Therefore, relative density is a controlling factor for network connectivity and the mechanical strength of np-Au.

2.4. The Origin of High Relative Density in Dealloyed Nanoporous Gold

Most np-Au dealloyed from Au-Ag precursors had relative densities between 25 to 30%.^[16] Especially, at the same 25:75 atomic ratio in Au-Ag, when the residual Ag is required to be low (e.g., ≤ 1 at%), a low relative density less than 30% is almost inevitable in syntheses, such as 25% in Figure 3e and 26% in ref. [13]. Differently, here, all dealloyed np-Au from Au₂₅Ni₇₅ have relative densities above 34%.

The mysteriously higher relative density originated from the smaller atomic radius of the sacrificing element Ni (1.3758 Å) than Ag (1.5901 Å).^[54] Quantitatively, we establish a general model to predict the relative density of np-Au dealloyed from binary alloys, which can be conveniently extended to ternary alloys and other alloy systems

$$\varphi = \frac{V_0 - n(1-x-R)\Omega_2}{(1-S)V_0} \quad (2)$$

$$V_0 = n[x\Omega_1 + (1-x)\Omega_2] \quad (3)$$

where φ , V_0 , n , x , R , and S represent the relative density of np-Au, unit cell volume of the precursor, number of atoms in the unit cell, Au atomic ratio in the precursor, residual sacrificing element content in np-Au, and volume shrinkage of np-Au in comparison to the precursor, respectively. $\Omega_1 = (4\pi/3)r_1^3$ and $\Omega_2 = (4\pi/3)r_2^3$ are atomic volume of Au and the sacrificing element, and r is the corresponding atomic radius. Equation (2) is established here by considering the key variables that can affect the relative density of np-Au, i.e., V_0 , x , R , and S . V_0 will change with the composition of the precursor, we use Zen's mixture rule for atomic volumes^[55] to obtain Equation (3). Noting that a similar but different equation to estimate the porosity of nanoporous Ag obtained by reduction-induced decomposition (RID) rather than dealloying was reported, without considering the residual element content.^[45c]

Figure 5a shows two baselines of relative densities calculated by Equation (2) for np-Au dealloyed from Au_{*x*}Ni_(1-*x*) and Au_{*x*}Ag_(1-*x*), at zero residual Ni or Ag content ($R = 0\%$) and zero volume shrinkage ($S = 0\%$). The region of practical interests normally locates at $20\% \leq x \leq 35\%$, beyond which monolithic crack-free np-Au may not be obtained from Au_{*x*}Ag_(1-*x*).^[13] In Figure 5a, $\varphi \approx x$ for Au_{*x*}Ag_(1-*x*) due to the almost identical atomic radius between Au and Ag; while $\varphi > x$ for Au_{*x*}Ni_(1-*x*) due to the smaller atomic radius of Ni than Au. In the practical

region, φ dealloyed from Au_{*x*}Ni_(1-*x*) is one-third larger than that dealloyed from Au_{*x*}Ag_(1-*x*), i.e., from $\varphi = 20$ and 35% increased to $\varphi = 28$ and 45%. This advantage is striking because the yielding strength of np-Au is proportional to $\varphi^{3/2}$ according to Gibson-Ashby,^[15] plus additional gains for better network connectivity when $\varphi > 30\%$ threshold.^[16-17]

In experiments, residual Ni or Ag content can be < 1 at% after sufficient dealloying (here, it is rounded to $R = 0\%$ in the calculation). Volume shrinkage (S) can vary from several to tens of percentages during dealloying or post-annealing.^[13] Figure 5b shows that the calculated φ from Equation (2) (curves) are in excellent agreement with experiments (symbols) obtained by Zandersons et. al.^[13] for np-Au dealloyed from various Au_{*x*}Ag_(1-*x*) precursors when R and S are the same between the prediction and experiments; except one data point at $x = 35\%$, where the residual Ag should < 1 at% from our prediction, while R was mentioned to be $\approx 3\%$ in experiments after 25 days of chemical dealloying in 65 wt.% HNO₃.^[13] Noting that S was not directly provided in ref. [13], but it can be indirectly obtained from the provided densification parameter, $\nu = \varphi/x$. Because the atomic radius of Au (1.5884 Å) is very close to Ag (1.5901 Å),^[54] we have $\Omega_1 \approx \Omega_2$. Substituting this into Equation (2) and (3), we obtain S from ν (listed in Table S1 in the Supporting Information)

$$S = 1 - \frac{1}{\nu} - \frac{R}{\varphi} \quad (4)$$

The consistency between our predicted relative densities and the experimental values for np-Au dealloyed for Au_{*x*}Ag_(1-*x*) validate our model. It is then used to compare our experimental obtained φ for Au_{*x*}Ni_(1-*x*) (listed in Table S2 in the Supporting Information). Figure 5c shows the calculated φ values also sensibly agree with experiments for np-Au dealloyed from Au₂₅Ni₇₅ at the same R and S .

From Figure 5b,c, φ increases with the increment of either R or S . At a fixed element ratio of 25:75 in the precursor, Figure 5d shows that both calculated and experimental obtained φ for Au₂₅Ni₇₅ is much larger than that for Au₂₅Ag₇₅, i.e., φ increases from 25% to 34% at $S = 0\%$ and $R = 0\%$, and φ increases from 28% to 38% at $S = 10\%$ and $R = 0\%$. By increasing S , the large differences in φ between Au₂₅Ni₇₅ and Au₂₅Ag₇₅ are maintained. Figure 5d explicitly shows that the relative density of np-Au dealloyed from Au_{*x*}Ni_(1-*x*) is intrinsically and significantly larger than that dealloyed from Au_{*x*}Ag_(1-*x*).

3. Conclusions

Bulk monolithic np-Au is dealloyed from single-phase Au₂₅Ni₇₅ solid-solution for the first time. By using a sacrificing element, Ni, that has a smaller atomic radius than Ag of the conventional Au₂₅Ag₇₅ precursors, the relative density of np-Au is increased from 25–28% to 35–36% in our experiments, well above the 30% threshold for network connectivity. Benefiting from the low critical dealloying potential (≈ 0.6 V vs SHE) that is a half of Au-Ag (≈ 1.2 V vs SHE), Au anodic oxidation and oxygen evolution are avoided at the dealloying front, which promotes ≈ 10 times faster dealloying rate and low residual Ni content < 1 at%. Hydrochloric

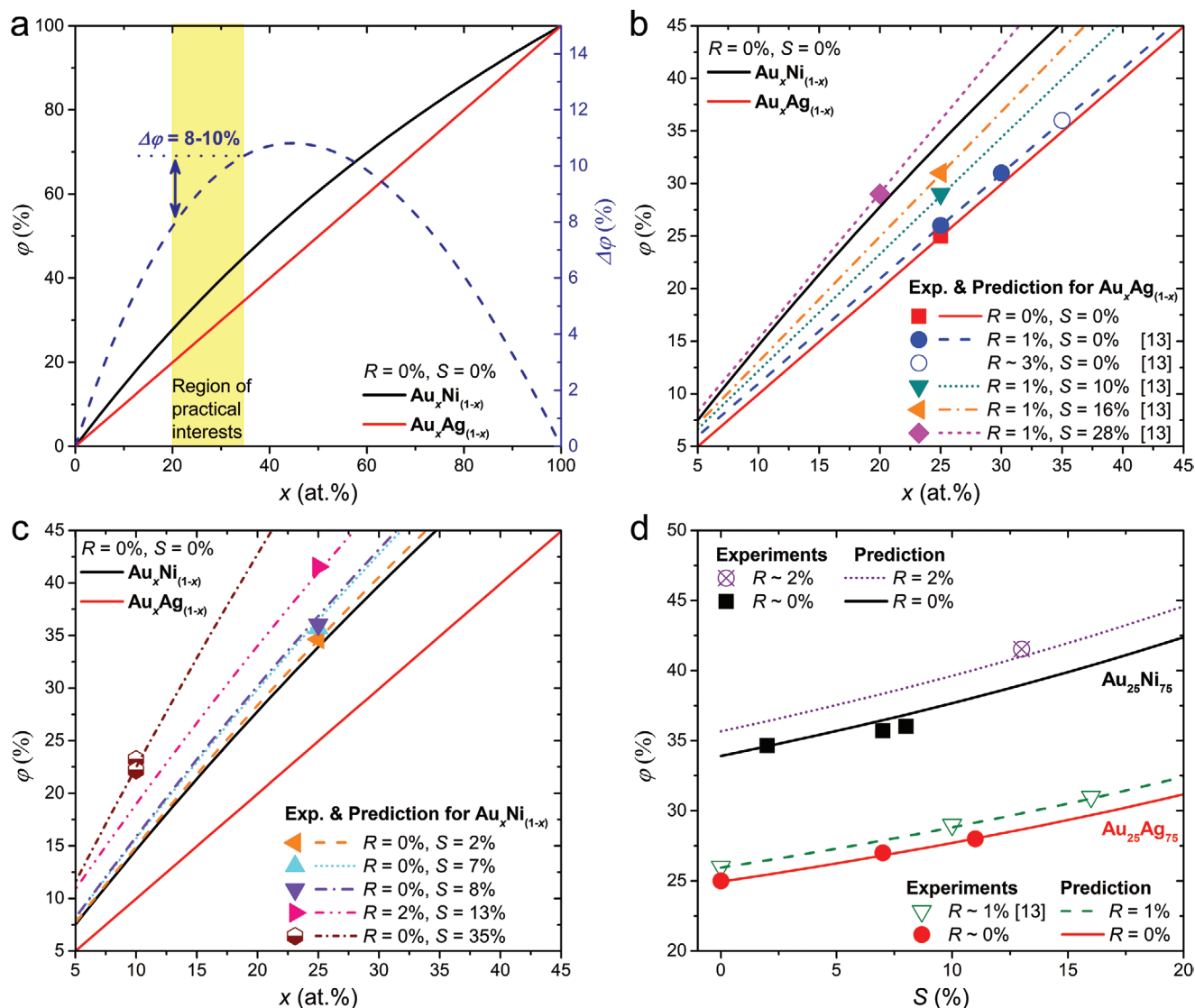


Figure 5. Predicted and experimental obtained relative densities of np-Au dealloyed from $\text{Au}_x\text{Ni}_{(1-x)}$ and $\text{Au}_x\text{Ag}_{(1-x)}$. a) Predicted relative density (φ) versus Au content of the precursor (x), at zero residual Ni or Ag content in np-Au ($R = 0\%$) and zero volume shrinkage of np-Au ($S = 0\%$). The blue curve shows φ differences. b) φ of np-Au dealloyed from $\text{Au}_x\text{Ag}_{(1-x)}$. c) φ of np-Au dealloyed from $\text{Au}_x\text{Ni}_{(1-x)}$. Some experimental data come from ref. [13]. d) φ versus volume shrinkage of np-Au dealloyed from $\text{Au}_{25}\text{Ni}_{75}$ and $\text{Au}_{25}\text{Ag}_{75}$. Curves represent predictions by Equation (2), and symbols represent experimental data listed in Tables S1 and S2 in the Supporting Information.

acid is also essential to prevent surface passivation. Negligible coarsening-induced strain-shift is found in bulk np-Au actuators working in both acidic and alkaline electrolytes during long-term reversible actuation (≥ 10 h), which shows remarkable structure stability. The actuation amplitude is ≈ 10 times larger than that dealloyed from Au-Ag with the same ligament size due to more effective ligaments, rather than dangling ligaments, to contribute to macroscopic volume change. The thermal and mechanical robustness of np-Au is confirmed by a two-order slower coarsening rate than conventional np-Au coarsened from the same ligament size (120 nm) and high macroscopic yielding strength (45 MPa) without the early onset of plastic yielding.

A general model to predict the relative density of np-Au dealloyed from binary alloys is established, which can be extended to other alloy systems. The predictions are validated by experiments,

which show that $\text{Au}_x\text{Ni}_{(1-x)}$ generate one-third more relative densities in np-Au than $\text{Au}_x\text{Ag}_{(1-x)}$ at the practical region in x for crack-free monolith np-Au formation. Single-phase Au-Ni solid-solution could be obtained in all compositions, which opens a rich direction for high relative density np-Au dealloyed from a new type of precursor. Methods and equations presented here could become a general strategy to increase relative densities in other dealloyed nanoporous metals, while high relative density is the key for network connectivity, mechanical strength, and nanostructure robustness for functionality.

4. Experimental Section

Precursor Fabrication: $\text{Au}_{25}\text{Ni}_{75}$ alloy ingots were cast from pure Au and Ni metals by an arc melter (MAM-1, Edmund Bühler) within argon. The

ingots were annealed at 900 °C for 24 h in the air, and then quenched in water from 900 °C to room temperature. The ingots were then cut by a diamond wire saw into 3D mm-sized precursors, with sizes in the range of $1.38 \pm 0.15 \text{ mm} \times 1.01 \pm 0.32 \text{ mm} \times 0.72 \pm 0.17 \text{ mm}$.

Electrochemical Dealloying: Precursors were dealloyed at constant potentials in an electrochemical cell controlled by a potentiostat (Autolab, PGSTAT302N). The cell was filled with 200 mL 1 M HCl and the temperature was controlled at constant by circulating water within the outer lining of the cell from a water bath. The precursor was hanged at the middle of the electrolyte by a gold-foil holder, which was electrically connected to the working electrode of the potentiostat by a gold wire. A standard hydrogen electrode (HydroFlex®, Gaskatel GmbH) acted as the reference electrode, and a curled Ag wire acted as a counter electrode. Dealloying was finished when the current was reduced below 10 μA .

Details for $\text{Au}_{25}\text{Ag}_{75}$ dealloying can be found in one of the authors' Ph.D. thesis.^[51] $\text{Au}_{25}\text{Ag}_{75}$ cylinders ($\approx 1.0 \text{ mm}$ diameter \times 1.0 height) were first electrochemically dealloyed in 1 M HClO_4 at 1.25 V versus SHE, and post-dealloyed in the same electrolyte at 1.35 V versus SHE for 20 min. It was followed by 20 cyclic voltammetry cycles within [0.1, 1.6] V versus SHE at 5 mV s^{-1} and stopped at 0.8 V versus SHE to further reduce residual Ag content $< 1 \text{ at}\%$ and to reduce the oxidized Au surface.

Electron Microscopy Characterization: The precursor and np-Au were analyzed by X-ray diffraction in a Bruker D8 powder diffractometer (Cu $K\alpha$). Nanoporous structures were observed by SEM carried out in a Zeiss Supra 55 VP FEG-SEM combined with EDX. Photos of the samples were captured by optical microscopy (Leica M205C, Germany). To observe annealed morphology, np-Au dealloyed from $\text{Au}_{25}\text{Ni}_{75}$ were annealed in a vacuum furnace (MILA-5000, ULVAC) at $\approx 10^{-6}$ mbar at 300 °C for 3 h; np-Au dealloyed from $\text{Au}_{25}\text{Ag}_{75}$ were annealed in the air for 5, 10, 20 min, respectively. Although np-Au annealed in the air may coarsen slower than in the vacuum due to possible surface oxidation, the coarsening rate is still far slower than np-Au dealloyed from $\text{Au}_{25}\text{Ni}_{75}$.

Mechanical Characterization: Uniaxial compression tests were conducted on a universal testing machine (Zwick 1474) at a constant engineering strain rate of 10^{-4} s^{-1} with a pre-load of 0.3 N at the beginning of the measurement for close contact between sample and pushrod.

Electrochemical Actuation Measurement: The linear actuation strain of cuboid-shaped bulk np-Au was measured in situ in an electrochemical cell, combined with a computer-controlled dilatometer (Linseis, L75 vertical dilatometer) and a potentiostat (Autolab, PGSTAT302N). A glass pushrod that was connected with the displacement sensor of the dilatometer had a constant compressive pressure ($\approx 0.2 \text{ MPa}$) on the top surface of the sample to maintain close contact between the pushrod and the sample. The electrochemical cell was filled with either 1 M NaOH or 1 M H_2SO_4 , as noticed in the main text. The np-Au served as a working electrode and a piece of carbon cloth served as a counter electrode. During actuation in 1 M H_2SO_4 , a commercial standard hydrogen electrode (HydroFlex®, Gaskatel GmbH) acted as a reference electrode. During actuation in 1 M NaOH, a commercial Hg/HgO reference electrode ($\approx 0.098 \text{ V}$ versus SHE, Sensortechnik Meinsberg, Germany) was used, and the electrode potentials were converted against the standard hydrogen electrode.

Supporting Information

Supporting Information is available from the Wiley Online Library or from the author.

Acknowledgements

Part of this research was conducted during C.C.'s visit to the Hamburg University of Technology. C.C. thanks Humboldt Research Fellowship from Alexander von Humboldt Foundation, Germany. Correction added

on 17 December 2021, after first online publication: Projekt Deal funding statement has been added.

Open access funding enabled and organized by Projekt DEAL.

Conflict of Interest

The authors declare no conflict of interest.

Data Availability Statement

The data that support the findings of this study are available from the corresponding author upon reasonable request.

Keywords

charge-induced reversible strain, coarsening, electrochemical actuators, electrochemical dealloying, nanoporous gold

Received: August 1, 2021

Revised: August 15, 2021

Published online: August 31, 2021

- [1] a) J. Erlebacher, M. J. Aziz, A. Karma, N. Dimitrov, K. Sieradzki, *Nature* **2001**, *410*, 450; b) Q. Chen, K. Sieradzki, *Nat. Mater.* **2013**, *12*, 1102; c) Z. Lu, C. Li, J. Han, F. Zhang, P. Liu, H. Wang, Z. Wang, C. Cheng, L. Chen, A. Hirata, T. Fujita, J. Erlebacher, M. Chen, *Nat. Commun.* **2018**, *9*, 276.
- [2] a) X. Wu, G. He, Y. Ding, *Electrochem. Energy Rev.* **2020**, *3*, 541; b) Z. Qi, M. M. Biener, A. R. Kashi, S. Hunegnaw, A. Leung, S. Ma, Z. Huo, K. P. Kuhl, J. Biener, *J. CO2 Util.* **2021**, *45*, 101454.
- [3] K. Sieradzki, N. Dimitrov, D. Movrin, C. McCall, N. Vasiljevic, J. Erlebacher, *J. Electrochem. Soc.* **2002**, *149*, B370.
- [4] L. Luhrs, C. Soyarslan, J. Markmann, S. Bargmann, J. Weissmüller, *Scr. Mater.* **2016**, *110*, 65.
- [5] a) H. J. Jin, J. Weissmüller, *Science* **2011**, *332*, 1179; b) L. Luhrs, B. Zandersons, N. Huber, J. Weissmüller, *Nano Lett.* **2017**, *17*, 6258.
- [6] M. Wang, A. C. Meng, J. Fu, A. C. Foucher, R. Serra-Maia, E. A. Stach, E. Detsi, J. H. Pikul, *ACS Appl. Mater. Interfaces* **2021**, *13*, 13097.
- [7] X. Y. Lang, H. T. Yuan, Y. Iwasa, M. W. Chen, *Scr. Mater.* **2011**, *64*, 923.
- [8] Z. Q. Peng, S. A. Freunberger, Y. H. Chen, P. G. Bruce, *Science* **2012**, *337*, 563.
- [9] J. A. Hondred, Z. T. Johnson, J. C. Claussen, *J. Mater. Chem. C* **2020**, *8*, 11376.
- [10] J. Biener, A. Wittstock, L. A. Zepeda-Ruiz, M. M. Biener, V. Zielasek, D. Kramer, R. N. Viswanath, J. Weissmüller, M. Baumer, A. V. Hamza, *Nat. Mater.* **2009**, *8*, 47.
- [11] R. N. Viswanath, V. A. Chirayath, R. Rajaraman, G. Amarendra, C. S. Sundar, *Appl. Phys. Lett.* **2013**, *102*, 253101.
- [12] H. J. Jin, X. L. Wang, S. Parida, K. Wang, M. Seo, J. Weissmüller, *Nano Lett.* **2010**, *10*, 187.
- [13] B. Zandersons, L. Luhrs, Y. Li, J. Weissmüller, *Acta Mater.* **2021**, *215*, 116979.
- [14] a) S. Shi, Y. Li, B.-N. Ngo-Dinh, J. Markmann, J. Weissmüller, *Science* **2021**, *371*, 1026; b) N. Mameka, K. Wang, J. Markmann, E. T. Lilleodden, J. Weissmüller, *Mater. Res. Lett.* **2016**, *4*, 27.
- [15] L. J. Gibson, M. F. Ashby, *Cellular Solids: Structure and Properties*, Cambridge University Press, Cambridge **1997**.

- [16] Y. Li, B. N. D. Ngo, J. Markmann, J. Weissmüller, *Phys. Rev. Mater.* **2019**, *3*, 076001.
- [17] a) H. Xie, H. Guan, L.-Z. Liu, H.-J. Jin, *Acta Mater.* **2021**, *209*, 116806; b) J. Erlebacher, R. C. Newman, K. Sieradzki, in *Nanoporous Gold: From an Ancient Technology to a High-Tech Material* (Eds: A. Wittstock, J. Biener, J. Erlebacher, M. Baumer), Royal Society of Chemistry, **2012**.
- [18] Y. Zhong, J. Markmann, H. J. Jin, Y. Ivanisenko, L. Kurmanaeva, J. Weissmüller, *Adv. Eng. Mater.* **2014**, *16*, 389.
- [19] Z. H. Zhang, Y. Wang, Z. Qi, C. Somsen, X. G. Wang, C. C. Zhao, *J. Mater. Chem.* **2009**, *19*, 6042.
- [20] J. F. Huang, I. W. Sun, *Adv. Funct. Mater.* **2005**, *15*, 989.
- [21] J. Xu, Y. Wang, Z. Zhang, *J. Phys. Chem. C* **2012**, *116*, 5689.
- [22] E. Rouya, M. L. Reed, R. G. Kelly, H. Bart-Smith, M. Begley, G. Zangari, *ECS Trans.* **2007**, *6*, 41.
- [23] in *ASM Handbook, Volume 3: Alloy Phase Diagrams*, Vol. 3 (Eds: H. Okamoto, M. E. Schlesinger, E. M. Mueller), ASM International, **2016**, p. 164.
- [24] E. R. Jette, F. Foote, *J. Chem. Phys.* **1935**, *3*, 605.
- [25] J.-C. Zhao, M. R. Notis, *Metall. Trans. A* **1999**, *30*, 707.
- [26] J. Erlebacher, R. C. Newman, K. Sieradzki, in *Nanoporous Gold: From an Ancient Technology to a High-Tech Material* (Eds: A. Wittstock, J. Biener, J. Erlebacher, M. Baumer), Royal Society of Chemistry, Cambridge, UK **2012**.
- [27] S. Cherevko, A. A. Topalov, I. Katsounaros, K. J. J. Mayrhofer, *Electrochem. Commun.* **2013**, *28*, 44.
- [28] M. Haensch, M. Graf, W. Wang, A. Nefedov, C. Wöll, J. Weissmüller, G. Wittstock, *ACS Appl. Nano Mater.* **2020**, *3*, 2197.
- [29] Y. Ding, Y.-J. Kim, J. Erlebacher, *Adv. Mater.* **2004**, *16*, 1897.
- [30] C. Cheng, L. Lührs, T. Krekeler, *Adv. Electron. Mater.* **2021**, 2100381.
- [31] Image J, a software designed by W. Rasband, version 1.53c, NIH: USA, public domain, <http://imagej.nih.gov/ij/>
- [32] J. M. Dona, J. Gonzalez-Velasco, *J. Phys. Chem. C* **1993**, *97*, 4714.
- [33] R. M. Carranza, M. A. Rodríguez, *NPG Mater. Degrad.* **2017**, *1*, 9.
- [34] H. J. Jin, S. Parida, D. Kramer, J. Weissmüller, *Surf. Sci.* **2008**, *602*, 3588.
- [35] M. Pourbaix, *Atlas of Electrochemical Equilibria in Aqueous Solutions*, Pergamon Press Ltd, London **1966**.
- [36] R. Córdova O, M. E. Martins, A. J. Arvía, *Electrochim. Acta* **1980**, *25*, 453.
- [37] F. Weigend, F. Evers, J. Weissmüller, *Small* **2006**, *2*, 1497.
- [38] C. Cheng, A. H. W. Ngan, *ACS Nano* **2015**, *9*, 3984.
- [39] S. H. Lee, J. C. Rasaiah, *J. Chem. Phys.* **2011**, *135*, 124505.
- [40] C. Cheng, J. Weissmüller, A. H. W. Ngan, *Adv. Mater.* **2016**, *28*, 5315.
- [41] B. Roschning, J. Weissmüller, *Adv. Mater. Interfaces* **2020**, *7*, 2001415.
- [42] N. Huber, R. N. Viswanath, N. Mameka, J. Markmann, J. Weissmüller, *Acta Mater.* **2014**, *67*, 252.
- [43] P. S. Germain, W. G. Pell, B. E. Conway, *Electrochim. Acta* **2004**, *49*, 1775.
- [44] C. Cheng, P. S. Grant, L. Lührs, *Adv. Electron. Mater.* **2020**, *6*, 1900364.
- [45] a) G. Pia, F. Delogu, *Acta Mater.* **2015**, *99*, 29; b) L. H. Qian, M. W. Chen, *Appl. Phys. Lett.* **2007**, *91*, 083105; c) C. Wang, Q. Chen, *Chem. Mater.* **2018**, *30*, 3894.
- [46] C. Herring, *J. Appl. Phys.* **1950**, *21*, 301.
- [47] J. Erlebacher, *Phys. Rev. Lett.* **2011**, *106*, 225504.
- [48] A. J. Melmed, *J. Appl. Phys.* **1967**, *38*, 1885.
- [49] a) I. Beszeda, I. A. Szabó, E. G. Gontier-Moya, *Appl. Phys. A* **2004**, *78*, 1079; b) A. Surrey, D. Pohl, L. Schultz, B. Rellinghaus, *Nano Lett.* **2012**, *12*, 6071.
- [50] J. Biener, A. M. Hodge, J. R. Hayes, C. A. Volkert, L. A. Zepeda-Ruiz, A. V. Hamza, F. F. Abraham, *Nano Lett.* **2006**, *6*, 2379.
- [51] L. Lührs, *PhD Thesis*, Hamburg University of Technology **2020**.
- [52] K. Wang, A. Kobler, C. Kubel, H. Jelitto, G. Schneider, J. Weissmüller, *NPG Asia Mater* **2015**, *7*, 187.
- [53] K. Hu, M. Ziehmer, K. Wang, E. T. Lilleodden, *Phil. Mag.* **2016**, *96*, 3322.
- [54] V. A. Lubarda, *Mech. Mater.* **2003**, *35*, 53.
- [55] E.-a. Zen, *Am. Mineralogist* **1956**, *41*, 523.